(Fig. 1) [33,34]. Fig. 2A presents a TEM image of ferucarbotran alone, the size of which is consistent with reported values [36,37]. Successful loading of ferucarbotran, seen as small black dots of approximately 30 nm in diameter, into the PICsome was confirmed in Fig. 2B. In this unstained TEM image, the ferucarbotran particles can be seen to overlap dark gray shadows (diameter approximately 100 nm), that correspond to the PICsomes. It is noteworthy that unencapsulated SPIOs were rarely observed in the SPIO-Cy5-PICsome samples, indicating an almost complete removal of the SPIOs by preparative GPC. Additionally, in the stained TEM images (Fig. S1), vesicular structures of a similar size to the shadows in Fig. 2B were found. The DLS result demonstrated a narrow size distribution for the SPIO-Cy5-PICsomes (Fig. 2C, average diameter = 102 nm, polydispersity index (PDI) = 0.056), that was consistent with the size of the black dots in the TEM images. The SPIO-Cy5-PICsomes were large enough to contain multiple SPIO nanoparticles, and multiple SPIOs encapsulated in a single Nano-PICsome were occasionally observed (Fig. 2B, white arrow).

3.2. In vitro R_2

The dependence of R_2 on iron concentration is shown in Fig. 2D and E. The R_2 of SPIO-Cy5-PICsomes was approximately twice as large as that of ferucarbotran (20 µM SPIO-Cy5-PICsomes: 15.86 ± 0.60 s^{-1}, ferucarbotran: 7.89 ± 0.67 s^{-1}). The r_2 of the SPIO-Cy5-PICsomes and ferucarbotran were 663 ± 28 mM^{-1} s^{-1} and 261 ± 30 mM^{-1} s^{-1}, respectively. There are two factors that may contribute to the larger r_2 of the SPIO-Cy5-PICsomes. The first is that, as shown in the TEM image (Fig. 2B), some of the SPIO-Cy5-PICsomes contain multiple SPIO nanoparticles. Having two or more SPIO nanoparticles in close proximity will perturb the shape of the surrounding magnetic field gradient and potentially increase the observed r_2. This effect has been shown in
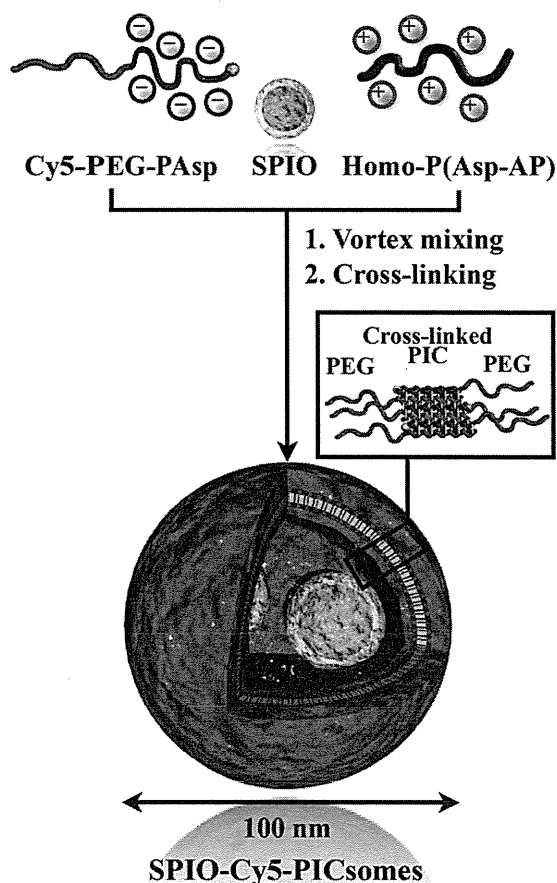

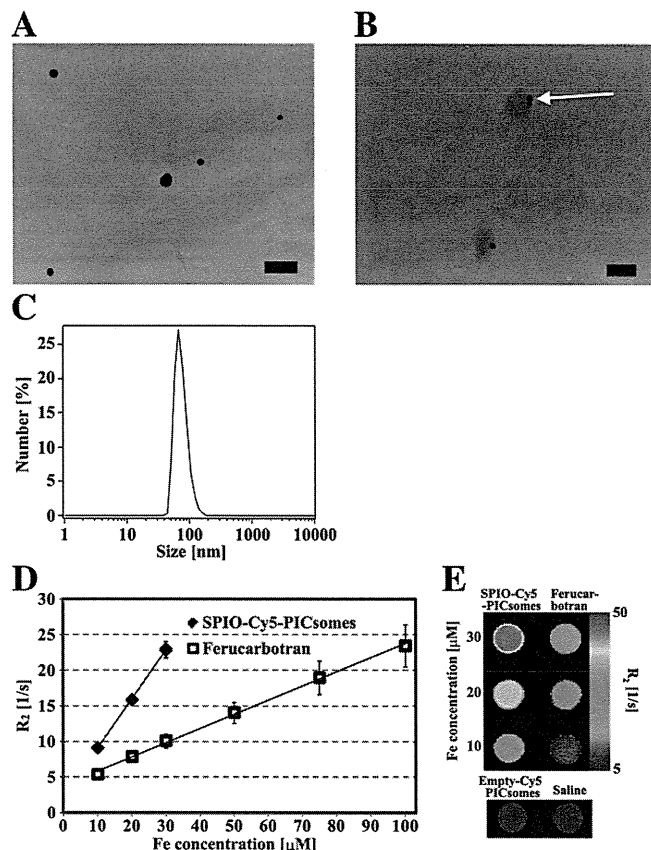Fig. 1. Schematic representation of the SPIO-Cy5-PICsome preparation.

Fig. 2. Results of the *in vitro* TEM, DLS, and R_2 measurements. TEM images of (A) ferucarbotran and (B) SPIO-Cy5-PICsomes. The scale bar is 100 nm. (C) A typical size distribution for SPIO-Cy5-PICsomes determined by DLS. (D) Concentration dependence of R_2s. A straight line fit for the SPIO-Cy5-PICsomes gave y = 0.69 x + 2.16 (R^2 = 0.9998), and for ferucarbotran y = 0.20 x + 3.86 (R^2 = 0.998). (E) Representative R_2 mapping of SPIO-Cy5-PICsomes, ferucarbotran, empty Cy5-PICsomes and saline.

previous reports when the r_2 of aggregated SPIO or USPIO nanoparticles were enhanced in comparison to those of dispersed SPIO or USPIO nanoparticles [20,36–38]. The second factor that may influence the r_2 of SPIO-Cy5-PICsomes is the vesicle wall. As the experiment on empty Cy5-PICsomes indicated (Fig. 2E), the materials that compose the membrane do not affect r_2 significantly in comparison to pure saline. However, the paths of molecules diffusing through the field gradient near the SPIOs are influenced by the PIC layer or PEG chains on the PIC layer, and this could affect the observed r_2 [39,40].

3.3. In vivo analysis of tumor accumulation using MR and fluorescence imaging

Typical T$_2$-weighted MRI and fluorescence images of tumor before and up to 24 h after SPIO-Cy5-PICsome administration are shown in Fig. 3. In the MR images, signal reductions were observed in the tumors at 3 h after the administration. In fact, as shown in Fig. S2, signal alteration in the tumor was detected at 2 h after the administration, and the area of the signal alteration expanded over the next 4 h. The signal alteration was maintained until at least 24 h after administration (Fig. 3). MRI signal alteration in the tumor was in agreement with the *in vivo* fluorescence imaging (Fig. 3). The results were further confirmed by histological analysis of the tumor, with the results shown in Fig. 4. HE staining of the thin-sectioned tumor revealed rich vascularization of the tumor area without showing significant degeneration like necrosis. As detected from the fluorescence of the Cy5 dye, the accumulation of the SPIO-Cy5-PICsomes was especially high in tumor areas that showed clear MRI signal reduction (Figs. 3 and 4).
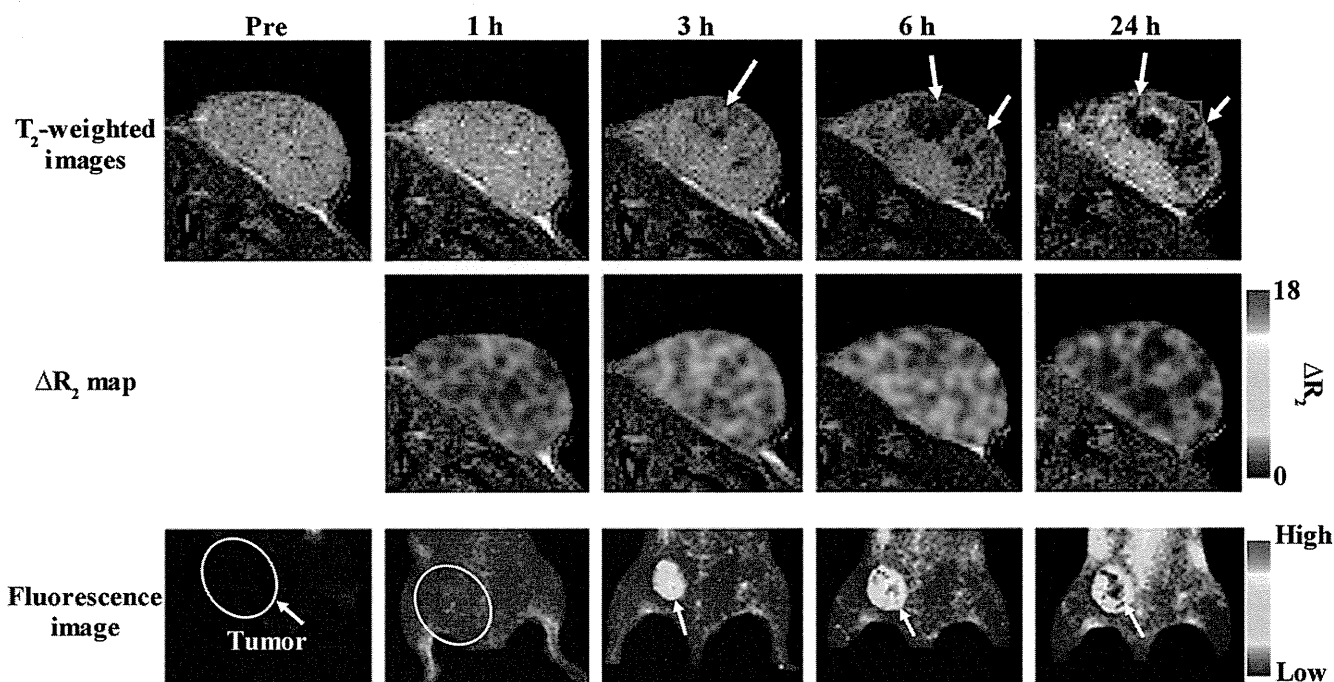
Fig. 3. Typical results of MRI and optical imaging of the *in vivo* tumor model. T_2-weighted MRIs (upper), ΔR_2 maps (middle), and fluorescence images (bottom) were obtained for up to 24 h after SPIO-Cy5-PICsome administration. The MRI signal in the tumor (arrows) was noticeably different 3 h after administration, and the area encompassing the signal change was clearly larger at 6 and 24 h after administration. For the fluorescence images, similar to the MRI the signal increased at 3 h after administration. The square in the 24 h T_2-weighted image corresponds to the area used for histological evaluation (see Fig. 4).

Fig. 5 shows how R_2 changed over the 24 h after SPIO-Cy5-PICsome or ferucarbotran administration. The R_2 of the tumor after SPIO-Cy5-PICsome administration gradually increased, and peaked with an increase of 30% at 6 h after administration in comparison to the values before administration (Fig. 5). At 24 h after administration, the R_2 remained at the same level as at 6 h. In contrast, the R_2 after ferucarbotran administration was significantly smaller than the values at 3, 6 and 24 h after SPIO-Cy5-PICsome administration (Fig. 5). These results are attributed to the facilitated EPR effect of SPIO-Cy5-PICsomes prolonging circulation in the bloodstream [34], and to the larger relaxivity (Fig. 2D). We also think that if our SPIO-Cy5-PICsomes are used, a tumor diagnosis might be made by comparing the MR images of 3 h and 24 h after administration.

Even though the pharmacokinetics of the SPIO-Cy5-PICsomes was not quantitatively investigated in this study, it is expected that they retain the same qualities as reported in our previous Cy5-PICsome study [34]. This is also supported by the low renal interaction of SPIO-Cy5-PICsomes, which was suggested by the negligible change in the MR signal intensity of kidney in the first 6 h after administration (Fig. S2), and sustained accumulation in the tumor between 3 and 24 h after administration (Figs. 3 and 5).

Changes in the body weight of the mice after SPIO-Cy5-PICsome or ferucarbotran administration are shown in Fig. S3. There were no significant changes during the week after SPIO-Cy5-PICsome administration. None of the animals exhibited other symptoms of systemic toxicity such as abnormal behavior or death after SPIO-Cy5-PICsome administration, even though a three times higher dose of SPIO-Cy5-PICsomes was administered (1.35 mg/kg Fe, Fig. S4).
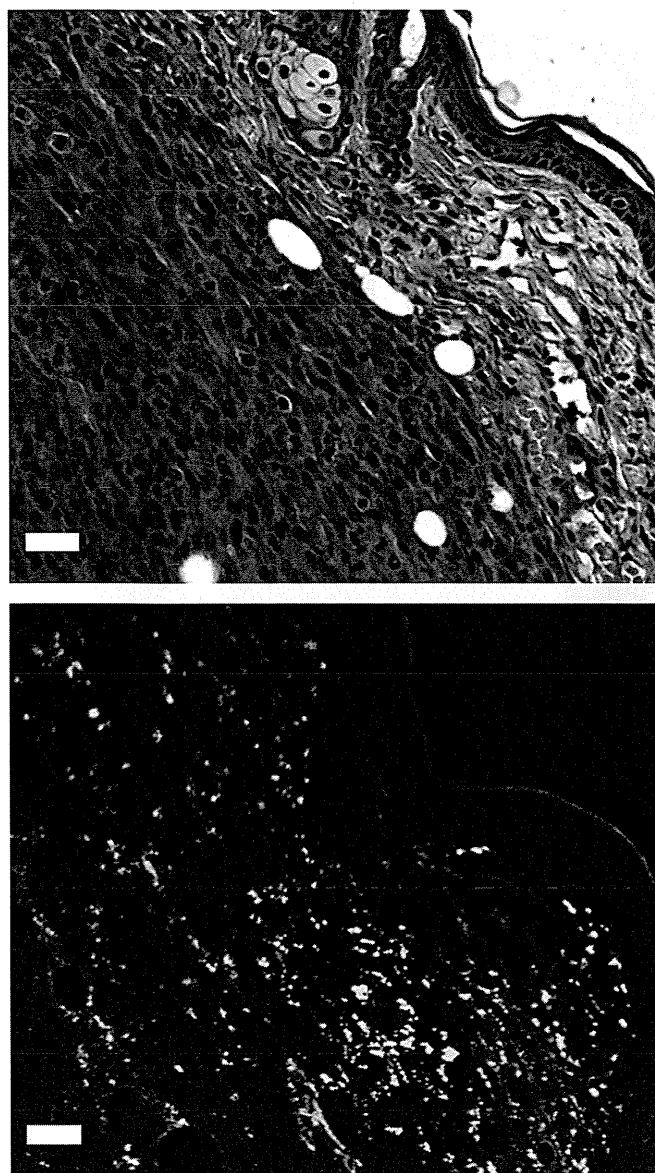
As noted in the Introduction, SPIO-loaded PEGylated nano-vesicles have several advantages, including longer circulation in the bloodstream and the potential to carry multiple iron-oxide particles, that enables strong signal enhancement in tumor [21–23]. It should also be noted that SPIO or USPIO-loaded PEGylated liposomes have been applied for tumor detection and evaluation of tumor treatment with

MRI [27–30]. It is our impression that PEGylated liposomes have characteristics that differ from Nano-PICsomes. The PEGylated liposomes have hydrophobic and non-permeable lipid membranes and can provide a platform for loading water-soluble drugs in a simple manner. However, the lipid membrane blocks communication between the inside and outside of the liposomes and it is technically difficult to conjugate with PEGs at a sufficiently high density. Therefore, liposomal formulations of this sort are not always favorable for *in vivo* sensing systems. On the other hand, Nano-PICsomes have a membrane that is permeable to low-molecular weight compounds, aids extremely prolonged circulation in the bloodstream, is a robust structure due to cross-linking, and forms a nano-particle of controllable diameter. These characteristics of Nano-PICsomes contribute to their potential to be carriers of sensor agents for probing the tissue environment *in vivo*; Nano-PICsomes are expected to accumulate selectively in tumors, working as highly sensitive MRI contrast agents.
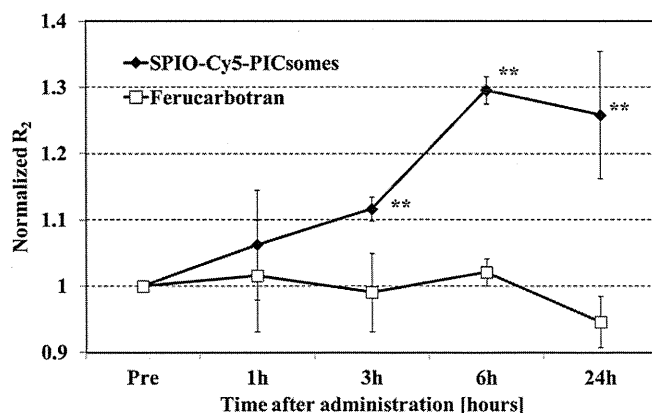
3.4. Detection of small and early-stage tumor

Fig. 6 presents the T_2-weighted images of a small and early-stage tumor (3 days after grafting, approximately 4 mm^3) before (Fig. 6A and C) and 24 h after (Fig. 6B and D) SPIO-Cy5-PICsome administration. MRI signal alteration was detectable *in vivo*. The Cy5 fluorescence signal observed in the tumor region was in agreement with the MRI signal alteration (Fig. 6E). When the skin covering the tumor region was incised, it was observed that several vessels were connected to the small and early-stage tumor (Fig. 6F and G). These results indicate that SPIO-Cy5-PICsomes accumulate, presumably due to the EPR effect, even in a small tumor that only had 3 days of *in vivo* growth in immunodeficient mice. Hence, if the micro-metastases are connected to the vasculature it is likely that SPIO-Cy5-PICsomes will accumulate in the tumor and aid early stage detection.

The *in vivo* detection of small tumors has been performed using other tomographic imaging modalities such as PET and single photon

Fig. 4. Histological analysis of the tumor sample shown in Fig. 3. The sample was serially sectioned and underwent HE staining (top), and fluorescence imaging of the Cy5 dye (bottom). The white dots in the fluorescence image indicate SPIO-Cy5-PICsomes. Scale bar, 50 nm (observed with a ×20 objective lens).

Fig. 5. Changes to the R_2 normalized by the value obtained before administration. The error bars denote the standard deviation. The closed diamonds correspond to tumors with SPIO-Cy5-PICsomes and the open squares to those with ferucarbotran. The level of significance was set at $p < 0.001$ (**) for a two-way ANOVA with Bonferroni correction.

4. Conclusion

Ferucarbotran-loaded unilamellar polyion complex vesicles, SPIO-Cy5-PICsomes, were developed as highly sensitive MRI contrast agents that accumulate in tumors. The properties of the SPIO-Cy5-PICsomes were evaluated both in vitro and in vivo. The transverse relaxivity of the SPIO-Cy5-PICsomes was 2.54 times higher than that of dispersed ferucarbotran. In a subcutaneously grafted colon 26 cancer model, significant alterations in the tumor MRI signals were reliably detected at 3 h after SPIO-Cy5-PICsome administration and maintained for 24 h. A small, early-stage tumor was also visualized using both in vivo MRI and fluorescence imaging. SPIO-loaded PICsomes allow small metastatic tumors to be detected and this may contribute to earlier identification for treatment in the clinic. In addition, these results indicate that loaded cross-linked PICsomes display similar pharmacokinetic behavior to unloaded cross-linked PICsomes, suggesting that PICsomes can be a versatile platform for nano-medicines. Looking ahead, anti-cancer-drug-loaded SPIO-PICsomes have potential therapeutic applications.
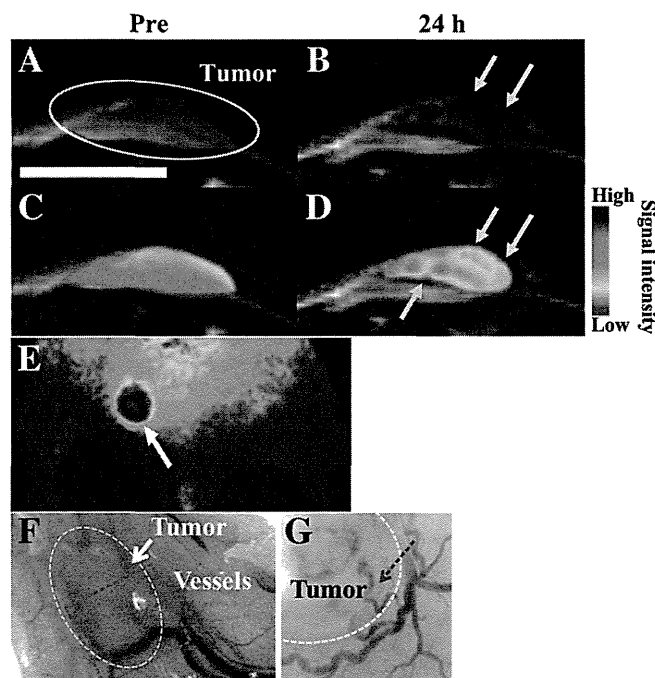
Supplementary data to this article can be found online at http://dx.doi.org/10.1016/j.jconrel.2013.03.016.

Acknowledgments

References

[1] M. Rudin, R. Weissleder, Molecular imaging in drug discovery and development, Nat. Rev. Drug Discov. 2 (2003) 123–131.
[2] T.F. Massoud, S.S. Gambhir, Molecular imaging in living subjects: seeing fundamental biological processes in a new light, Genes Dev. 17 (2003) 545–580.
[3] J.W. Bulte, D.L. Kraitchman, Iron oxide MR contrast agents for molecular and cellular imaging, NMR Biomed. 17 (2004) 484–499.
[4] Y.-X.J. Wang, Superparamagnetic iron oxide based MRI contrast agents: current status of clinical application, Quant. Imaging Med. Surg. 1 (2011) 35–40.
[5] J. Ward, K.S. Naik, J.A. Guthrie, D. Wilson, P.J. Robinson, Hepatic lesion detection: comparison of MR imaging after the administration of superparamagnetic iron oxide with dual-phase CT by using alternative-free response receiver operating characteristic analysis, Radiology 210 (1999) 459–466.

emission computed tomography (SPECT) [41,42]. The minimum size of a detectable tumor was approximately 1 mm in diameter, which is smaller than the tumor size detected in our trial. Although highly sensitive PET and SPECT imaging might be able to detect smaller tumors deeply seated within the body without requiring invasive procedures, it is difficult to determine the precise position of the tumor because of the limited spatial resolution (approximately 2–3 mm) of those modalities. The high sensitivity of MRI to SPIO nanoparticles has been used to observe the migration of groups of cells [43–48], and in some cases track the paths of single cells [49]. Combined with the high spatial resolution ($100 \times 100 \ \mu m^2$) of MRI, we therefore expect that SPIO-Cy5-PICsomes might be used to detect not only small tumors, but also their differential distribution due to variations in the micro-environment inside the tumor. Thus, SPIO-Cy5-PICsomes have the potential to provide novel diagnostic information for the clinic.

Fig. 6. Application of the SPIO-Cy5-PICsomes to small tumor detection. T_2-weighted MR images before (A, C) and at 24 h (B, D) after SPIO-Cy5-PICsome administration are shown. The tumor volume was approximately 4 mm^3. The scale bar has a length of 3 mm. The signal from the tumor (yellow arrows) at 24 h after the administration decreased from that before administration. In the fluorescence image (E) acquired 24 h after the administration, the signal from the tumor region (arrow) is higher than the signal from other regions. In the optical photo of the small tumor (F), several vessels can be seen connected to the tumor. It was confirmed that the vessels (blue dashed arrows) were connected to the tumor (outline highlighted by the white ellipse) in a higher magnification image (G) of the fixed tissue (blue square).

[6] J.H. Lim, D. Choi, S.K. Cho, S.H. Kim, W.J. Lee, H.K. Lim, C.K. Park, S.W. Paik, Y.I. Kim, Conspicuity of hepatocellular nodular lesions in cirrhotic livers at ferumoxides-enhanced MR imaging: importance of Kupffer cell number, Radiology 220 (2001) 669–676.

[7] A. Tanimoto, Y. Yuasa, H. Shinmoto, M. Jinzaki, Y. Imai, S. Okuda, S. Kuribayashi, Superparamagnetic iron oxide-mediated hepatic signal intensity change in patients with and without cirrhosis: pulse sequence effects and Kupffer cell function, Radiology 222 (2002) 661–666.

[8] Y. Lee, J.S. Lee, C.M. Kim, J.Y. Jeong, J.I. Choi, M.J. Kim, Area of paradoxical signal drop after the administration of superparamagnetic iron oxide on the T2-weighted image of a patient with lymphangitic metastasis of the liver, Magn. Reson. Imaging 26 (2008) 577–582.

[9] T. Schlorf, M. Meincke, E. Kossel, C.C. Gluer, O. Jansen, R. Mentlein, Biological properties of iron oxide nanoparticles for cellular and molecular magnetic resonance imaging, Int. J. Mol. Sci. 12 (2010) 12–23.

[10] Y. Matsumura, H. Maeda, A new concept for macromolecular therapeutics in cancer chemotherapy: mechanism of tumoritropic accumulation of proteins and the antitumor agent smancs, Cancer Res. 46 (1986) 6387–6392.

[11] Y. Tamaura, K. Takahashi, Y. Kodera, Y. Saito, Y. Inada, Chemical modification of lipase with ferromagnetic modifier—a ferromagnetic-modified lipase, Biotechnol. Lett. 8 (1986) 877–880.

[12] D.K. Kim, Y. Zhang, J. Kehr, T. Klason, B. Bjelke, M. Muhammed, Characterization and MRI study of surfactant-coated superparamagnetic nanoparticles administered into the rat brain, J. Magn. Magn. Mater. 225 (2001) 256–261.

[13] M. Kumagai, Y. Imai, T. Nakamura, Y. Yamasaki, M. Sekino, S. Ueno, K. Hanaoka, K. Kikuchi, T. Nagano, E. Kaneko, K. Shimokado, K. Kataoka, Iron hydroxide nanoparticles coated with poly(ethylene glycol)-poly(aspartic acid) block copolymer as novel magnetic resonance contrast agents for in vivo cancer imaging, Colloids Surf. B Biointerfaces 56 (2007) 174–181.

[14] H. Kojima, Y. Mukai, M. Yoshikawa, K. Kamei, T. Yoshikawa, M. Morita, T. Inubushi, T.A. Yamamoto, Y. Yoshioka, N. Okada, S. Seino, S. Nakagawa, Simple PEG conjugation of SPIO via an Au−S bond improves its tumor targeting potency as a novel MR tumor imaging agent, Bioconjug. Chem. 21 (2010) 1026–1031.

[15] G.B. Hong, J.X. Zhou, R.X. Yuan, Folate-targeted polymeric micelles loaded with ultrasmall superparamagnetic iron oxide: combined small size and high MRI sensitivity, Int. J. Nanomedicine 7 (2012) 2863–2872.

[16] N. Nasongkla, E. Bey, J. Ren, H. Ai, C. Khemtong, J.S. Guthi, S.F. Chin, A.D. Sherry, D.A. Boothman, J. Gao, Multifunctional polymeric micelles as cancer-targeted, MRI-ultrasensitive drug delivery systems, Nano Lett. 6 (2006) 2427–2430.

[17] H.J. Lee, K.S. Jang, S. Jang, J.W. Kim, H.M. Yang, Y.Y. Jeong, J.D. Kim, Poly(amino acid)s micelle-mediated assembly of magnetite nanoparticles for ultra-sensitive long-term MR imaging of tumors, Chem. Commun. (Camb.) 46 (2010) 3559–3561.

[18] J.S. Guthi, S.G. Yang, G. Huang, S. Li, C. Khemtong, C.W. Kessinger, M. Peyton, J.D. Minna, K.C. Brown, J. Gao, MRI-visible micellar nanomedicine for targeted drug delivery to lung cancer cells, Mol. Pharm. 7 (2010) 32–40.

[19] X. Yang, J.J. Grailer, I.J. Rowland, A. Javadi, S.A. Hurley, V.Z. Matson, D.A. Steeber, S. Gong, Multifunctional stable and pH-responsive polymer vesicles formed by heterofunctional triblock copolymer for targeted anticancer drug delivery and ultrasensitive MR imaging, ACS Nano 4 (2010) 6805–6817.

[20] W.I. Choi, J.Y. Kim, S.U. Heo, Y.Y. Jeong, Y.H. Kim, G. Tae, The effect of mechanical properties of iron oxide nanoparticle-loaded functional nano-carrier on tumor targeting and imaging, J. Control. Release 162 (2012) 267–275.

[21] J.X. Zhang, S.C. Dang, Y. Zhang, X. Sha, L.R. Zhang, C.S. Wei, M. Chen, D.L. Jiang, MRI shows clodronate-liposomes attenuating liver injury in rats with severe acute pancreatitis, Hepatobiliary Pancreat. Dis. Int. 9 (2010) 192–200.

[22] K. Katagiri, Y. Imai, K. Koumoto, T. Kaiden, K. Kono, S. Aoshima, Magnetoresponsive on-demand release of hybrid liposomes formed from $Fe_3 O_4$ nanoparticles and thermosensitive block copolymers, Small 7 (2011) 1683–1689.

[23] T. Toyota, N. Ohguri, K. Maruyama, M. Fujinami, T. Saga, I. Aoki, Giant vesicles containing superparamagnetic iron oxide as biodegradable cell-tracking MRI probes, Anal. Chem. 84 (2012) 3952–3957.

[24] M. Kumagai, T.K. Sarma, H. Cabral, S. Kaida, M. Sekino, N. Herlambang, K. Osada, M.R. Kano, N. Nishiyama, K. Kataoka, Enhanced in vivo magnetic resonance imaging of tumors by PEGylated iron-oxide-gold core-shell nanoparticles with prolonged blood circulation properties, Macromol. Rapid Commun. 31 (2010) 1521–1528.

[25] E.M. Shapiro, S. Skrtic, A.P. Koretsky, Sizing it up: cellular MRI using micron-sized iron oxide particles, Magn. Reson. Med. 53 (2005) 329–338.

[26] R. Kuhlpeter, H. Dahnke, L. Matuszewski, T. Persigehl, A. von Wallbrunn, T. Allkemper, W.L. Heindel, T. Schaeffter, C. Bremer, R2 and R2* mapping for sensing cell-bound superparamagnetic nanoparticles: in vitro and murine in vivo testing, Radiology 245 (2007) 449–457.

[27] M.S. Martina, J.P. Fortin, C. Menager, O. Clement, G. Barratt, C. Grabielle-Madelmont, F. Gazeau, V. Cabuil, S. Lesieur, Generation of superparamagnetic liposomes revealed as highly efficient MRI contrast agents for in vivo imaging, J. Am. Chem. Soc. 127 (2005) 10676–10685.

[28] A. Wijaya, K. Hamad-Schifferli, High-density encapsulation of Fe_3O_4 nanoparticles in lipid vesicles, Langmuir 23 (2007) 9546–9550.

[29] M.E. Meyre, G. Raffard, J.M. Franconi, E. Duguet, O. Lambert, C. Faure, Production of magnetic multilamellar liposomes as highly T2-efficient MRI contrast agents, Nanomedicine 7 (2011) 18–21.

[30] G. Bealle, R. Di Corato, J. Kolosnjaj-Tabi, V. Dupuis, O. Clement, F. Gazeau, C. Wilhelm, C. Menager, Ultra magnetic liposomes for MR imaging, targeting, and hyperthermia, Langmuir 28 (2012) 11834–11842.

[31] A. Koide, A. Kishimura, K. Osada, W.D. Jang, Y. Yamasaki, K. Kataoka, Semipermeable polymer vesicle (PICsome) self-assembled in aqueous medium from a pair of

oppositely charged block copolymers: physiologically stable micro-/nanocontainers of water-soluble macromolecules, J. Am. Chem. Soc. 128 (2006) 5988–5989.

[32] A. Kishimura, A. Koide, K. Osada, Y. Yamasaki, K. Kataoka, Encapsulation of myoglobin in PEGylated polyion complex vesicles made from a pair of oppositely charged block ionomers: a physiologically available oxygen carrier, Angew. Chem. Int. Ed Engl. 46 (2007) 6085–6088.

[33] Y. Anraku, A. Kishimura, M. Oba, Y. Yamasaki, K. Kataoka, Spontaneous formation of nanosized unilamellar polyion complex vesicles with tunable size and properties, J. Am. Chem. Soc. 132 (2010) 1631–1636.

[34] Y. Anraku, A. Kishimura, A. Kobayashi, M. Oba, K. Kataoka, Size-controlled long-circulating PICsome as a ruler to measure critical cut-off disposition size into normal and tumor tissues, Chem. Commun. (Camb.) 47 (2011) 6054–6056.

[35] P.J. Photos, L. Bacakova, B. Discher, F.S. Bates, D.E. Discher, Polymer vesicles *in vivo*: correlations with PEG molecular weight, J. Control. Release 90 (2003) 323–334.

[36] J.F. Berret, K. Yokota, M. Morvan, R. Schweins, Polymer-nanoparticle complexes: from dilute solution to solid state, J. Phys. Chem. B 110 (2006) 19140–19146.

[37] J. Yang, C.H. Lee, H.J. Ko, J.S. Suh, H.G. Yoon, K. Lee, Y.M. Huh, S. Haam, Multifunctional magneto-polymeric nanohybrids for targeted detection and synergistic therapeutic effects on breast cancer, Angew. Chem. Int. Ed Engl. 46 (2007) 8836–8839.

[38] S.-M. Lai, J.-K. Hsiao, H.-P. Yu, C.-W. Lu, C.-C. Huang, M.-J. Shieh, P.-S. Lai, Polyethylene glycol-based biocompatible and highly stable superparamagnetic iron oxide nanoclusters for magnetic resonance imaging, J. Mater. Chem. 22 (2012) 15160–15167.

[39] Q.L. Vuong, P. Gillis, Y. Gossuin, Monte Carlo simulation and theory of proton NMR transverse relaxation induced by aggregation of magnetic particles used as MRI contrast agents, J. Magn. Reson. 212 (2011) 139–148.

[40] E. Poselt, H. Kloust, U. Tromsdorf, M. Janschel, C. Hahn, C. Masslo, H. Weller, Relaxivity optimization of a PEGylated iron-oxide-based negative magnetic resonance contrast agent for T(2)-weighted spin-echo imaging, ACS Nano 6 (2012) 1619–1624.

[41] M. Brom, L. Joosten, P. Laverman, W.J. Oyen, M. Behe, M. Gotthardt, O.C. Boerman, Preclinical evaluation of 68Ga-DOTA-minigastrin for the detection of cholecystokinin-2/gastrin receptor-positive tumors, Mol. Imaging 10 (2011) 144–152.

[42] V. Patil, K. Gada, R. Panwar, A. Varvarigou, S. Majewski, A. Weisenberger, C. Ferris, Y. Tekabe, B.A. Khaw, Imaging small human prostate cancer xenografts after pretargeting with bispecific bombesin-antibody complexes and targeting with high specific radioactivity labeled polymer-drug conjugates, Eur. J. Nucl. Med. Mol. Imaging 39 (2012) 824–839.

[43] J.W. Bulte, S. Zhang, P. van Gelderen, V. Herynek, E.K. Jordan, I.D. Duncan, J.A. Frank, Neurotransplantation of magnetically labeled oligodendrocyte progenitors: magnetic resonance tracking of cell migration and myelination, Proc. Natl. Acad. Sci. U. S. A. 96 (1999) 15256–15261.

[44] M. Modo, D. Cash, K. Mellodew, S.C. Williams, S.E. Fraser, T.J. Meade, J. Price, H. Hodges, Tracking transplanted stem cell migration using bifunctional, contrast agent-enhanced, magnetic resonance imaging, Neuroimage 17 (2002) 803–811.

[45] A.S. Arbab, G.T. Yocum, H. Kalish, E.K. Jordan, S.A. Anderson, A.Y. Khakoo, E.J. Read, J.A. Frank, Efficient magnetic cell labeling with protamine sulfate complexed to ferumoxides for cellular MRI, Blood 104 (2004) 1217–1223.

[46] M. Babic, D. Horak, M. Trchova, P. Jendelova, K. Glogarova, P. Lesny, V. Herynek, M. Hajek, E. Sykova, Poly(L-lysine)-modified iron oxide nanoparticles for stem cell labeling, Bioconjug. Chem. 19 (2008) 740–750.

[47] J. Yang, J. Liu, G. Niu, K.C. Chan, R. Wang, Y. Liu, E.X. Wu, *In vivo* MRI of endogenous stem/progenitor cell migration from subventricular zone in normal and injured developing brains, Neuroimage 48 (2009) 319–328.

[48] K. Baeten, P. Adriaensens, J. Hendriks, E. Theunissen, J. Gelan, N. Hellings, P. Stinissen, Tracking of myelin-reactive T cells in experimental autoimmune encephalomyelitis (EAE) animals using small particles of iron oxide and MRI, NMR Biomed. 23 (2010) 601–609.

[49] E.M. Shapiro, S. Skrtic, K. Sharer, J.M. Hill, C.E. Dunbar, A.P. Koretsky, MRI detection of single particles for cellular imaging, Proc. Natl. Acad. Sci. U. S. A. 101 (2004) 10901–10906.

Clinical Cancer Research

AACR

Tissue redox activity as a hallmark of carcinogenesis: from early to terminal stages of cancer

Rumiana Bakalova, Zhivko Zhelev, Ichio Aoki, et al.

Updated version	Access the most recent version of this article at: doi:10.1158/1078-0432.CCR-12-3726
Author Manuscript	Author manuscripts have been peer reviewed and accepted for publication but have not yet been edited.

E-mail alerts	Sign up to receive free email-alerts related to this article or journal.
Reprints and Subscriptions	To order reprints of this article or to subscribe to the journal, contact the AACR Publications Department at pubs@aacr.org.
Permissions	To request permission to re-use all or part of this article, contact the AACR Publications Department at permissions@aacr.org.

Tissue redox activity as a hallmark of carcinogenesis: from early to terminal stages of cancer

Rumiana Bakalova,[1,2] Zhivko Zhelev,[1,3] Ichio Aoki,[1] Tsuneo Saga[1]

[1]Diagnostic Imaging Program, Molecular Imaging Center, National Institute of Radiological Sciences (NIRS), 4-9-1 Anagawa, Inage-ku, Chiba 263-8555, Japan
[2]Medical Faculty, Sofia University "St. Kliment Ohridski", 1 Koziak Str., Sofia 1407, Bulgaria
[3]Medical Faculty, Trakia University, 11 Armeiska Str., Stara Zagora, Bulgaria

Running title: Tissue redox activity as a hallmark of carcinogenesis

Translational relevance
This study directly relates to cancer diagnosis, the assessment of cancer progression (from early to terminal stage) and planning a therapeutic strategy. This study demonstrates that tissue redox balance is very sensitive to cancer development and can be used as a diagnostic marker of carcinogenesis. The method is simple and applicable on isolated tissue and blood specimens. The method demonstrates the potential for promising application in molecular imaging diagnostic *in vivo* on humans following the development of cell-penetrating nitroxide probes with high contrast, low toxicity and minimal side effects.

The most important observations are that the oxidative status of noncancerous tissues (even those distant from the primary tumor locus) increases with cancer progression and that these tissues become susceptible to oxidative stress and damage.

Abstract
Purpose: The study aimed to clarify the dynamics of tissue redox activity (TRA) in cancer progression and assess the importance of this parameter for therapeutic strategies.
Experimental design: The experiments were conducted on brain tissues of neuroblastoma-bearing, glioma-bearing and healthy mice. TRA was visualized *in vivo* by nitroxide-enhanced magnetic resonance imaging (MRI) on anesthetized animals or *in vitro* by electron paramagnetic resonance (EPR) spectroscopy on isolated tissue specimens. Two biochemical parameters were analyzed in parallel: tissue total antioxidant capacity (TTAC) and plasma levels of matrix metalloproteinases (MMPs).
Results: In the early stage of cancer, the brain tissues were characterized by a shorter-lived MRI signal than that from healthy brains (indicating a higher reducing activity for the nitroxide radical), which was accompanied by an enhancement of TTAC and MMP9 plasma levels. In the terminal stage of cancer, tissues in both hemispheres were characterized by a longer-lived MRI signal than in healthy brains (indicating a high oxidative activity) that was accompanied by a decrease in TTAC and an increase in the MMP2/MMP9 plasma levels. Cancer progression also affected the redox potential of tissues distant from the primary tumor locus (liver and lung). Their oxidative status increased in both stages of cancer.
Conclusions: The study demonstrates that tissue redox balance is very sensitive to the progression of cancer and can be used as a diagnostic marker of carcinogenesis. The study also suggests that the noncancerous tissues of a cancer-bearing organism are susceptible to oxidative damage and should be considered a therapeutic target.

Key words: cancer, tissue redox activity, total antioxidant capacity, metalloproteinases, magnetic resonance imaging

1

Introduction

Redox signaling plays a crucial role in carcinogenesis (1-4). The increase in cellular oxidants [e.g., reactive oxygen species (ROS) and reactive nitrogen species (RNS)] above a critical level triggers genomic instability and uncontrolled proliferation (1-7), which causes normal cells to become malignant.

Cancer cells are also characterized by an abnormal production of reducing equivalents as a result of accelerated glycolysis (Warburg effect) and the pentose phosphate cycle and by a rapid consumption of these reducers to maintain accelerated anabolism, which is necessary for cell proliferation and immortalization (1, 2, 7, 8). Cancer cells also require high amounts of antioxidants to maintain an ROS/RNS level that is below the threshold for the induction of apoptosis and cell death, but is sufficiently high to ensure genomic instability (1, 7, 9, 10). All of these processes provoke redox imbalance in cancer, which is a hallmark of carcinogenesis. The tissue redox status could be a diagnostic marker, a therapeutic target, and a marker for the evaluation and planning of a therapeutic strategy in real time.

The primary endogenous triggers of redox imbalance in cancer are defective mitochondria and NADPH oxidase complexes. These triggers are involved simultaneously in two processes that affect tissue redox status: (i) an excessive generation of ROS (in particular, superoxide and/or hydrogen peroxide) and RNS and (ii) an increased consumption of three of the major cellular reducers, as NADH, NADPH, and glutathione (1, 11-18). The high oxidative activity of cancerous tissue is known despite the hypoxia that occurs in solid tumors. The oxidative capacity of cancer cells is due to abnormal ROS/RNS levels and is not necessarily associated with a high oxygen tension. It is widely accepted that cancer cells are characterized by increased ROS/RNS production compared with that of normal cells that ensures genomic instability (1-15). ROS and RNS are involved in hypoxic signaling pathways and have important implications for the adaptation of cancer to oxidative stress, the induction of uncontrolled proliferation and immortalization.

Most likely, there is a significant difference between the redox activity of the tumor core and periphery in addition to tumors in different stages (i.e., early, intermediate and terminal) of development. However, there are methodological restrictions that hamper the visualization and evaluation of such a difference *in vivo*. There is no suitable sensor platform for real-time imaging of tissue redox activity that is characterized by high sensitivity and resolution.

Recently, we reported a noninvasive methodology for the estimation of tissue redox activity on intact mammals, allowing a differentiation of cancer development from normal (healthy) conditions (19-21). The method is based on the redox cycle of cell-penetrating nitroxide derivatives and their MRI and EPR contrast properties, which make them useful molecular sensors for tissue redox activity (Figure 1).

In vitro studies indicate that the contrast-enhancing nitroxide radical could be converted rapidly to the noncontrast-enhancing hydroxylamine and/or oxoammonium by different cellular compounds (e.g., free ions of transition metals, hydroxyl and hydroperoxyl radicals, ubiquinols, NAD(P)H, ascorbate/dehydroascorbate) (Figure 1) (22-28). In turn, hydroxylamine and oxoammonium are "superoxide dismutase mimetics" and could restore the nitroxide radical (22, 26, 29). The pKa value of 4.8 is reported for the equilibrium between superoxide anion and its protonated form, i.e., the hydroperoxyl radical. The interaction of oxoammonium with superoxide occurs at pH<4.5, whereas under physiological conditions (pH~7.4) the oxoammonium is reduced to hydroxylamine by NAD(P)H (26). The interaction of hydroxylamine with superoxide occurs at approximately pH 7.4 with the release of hydrogen peroxide and restoration of the radical form of the nitroxide (26). Ui et al. have

2

reported that the exposure to hydrogen peroxide inhibits the reduction of the nitroxide radical *in vivo*, and hydrogen peroxide reoxidizes hydroxylamine to the original radical form (22, 30). It appears that *in vivo*, nitroxide exists primarily in two forms: as a radical and as hydroxylamine. Various reducers and oxidizers are involved (directly or indirectly) in the formation of hydroxylamine, but only the interaction of hydroxylamine with superoxide and/or hydrogen peroxide appears to dominate *in vivo* as the process that restores the nitroxide radical and its MRI/EPR contrast.

Briefly, the nitroxide radical participates in electron transfer reactions with oxidizers and reducers with the formation of contrast-enhancing or noncontrast intermediate products (31-33). The rate constants of these reactions determine the intensity of the nitroxide-enhanced MRI/EPR signal in living cells and tissues. In healthy mammals, the intensity, duration and/or half-life of the nitroxide-enhanced MRI/EPR signal ($\tau_{1/2}$) in the selected region of interest (ROI) (e.g., cells, tissues, bloodstream) can be considered a reference value for the redox activity of the respective specimen in normal conditions (healthy organism) (19). Any significant deviation from this reference value indicates a redox imbalance, such as the high oxidative or reducing activity of cells, tissues or physiological fluids. In previous studies, we established that in cancer-bearing mammalian tissues, the intensity, duration and $\tau_{1/2}$ values were completely different from the respective reference values and that this parameter is a valuable diagnostic marker for carcinogenesis (19-21).

The EPR contrast of the nitroxide radical allows the determination of the exact concentration and redox status of the nitroxide derivative in the respective tissue and/or cells using EPR spectroscopy or imaging (EPRI) (31-35). The comparative analysis of the results, obtained using both imaging techniques, gives accurate information about the tissue redox activity *in vivo*.

The reduction/oxidation of nitroxide is spatially separated and occurs in (i) the bloodstream; (ii) the extracellular-extravascular space (EES) of the tissue; and (iii) the cells of the tissue. The MRI/EPR signal dynamics is a result of various factors and processes that occur simultaneously in the following three areas: (i) the lifetime of the nitroxide in the circulation, depending on its water solubility (35, 36); (ii) the reduction/oxidation of the nitroxide in the bloodstream, which is expected to be low in the plasma but sufficiently high in blood cells (if it penetrates cell membranes) (35, 36); (iii) the penetration and accumulation of the nitroxide in the EES and its reduction/oxidation, which is expected to be negligible; and (iv) the penetration and accumulation of the nitroxide in the cells of the tissue and its intracellular reduction/oxidation, which is expected to be substantial in comparison with the bloodstream and EES (20, 37). Tissue redox activity is a combination of the redox capacity of the extracellular (EES) and intracellular space of the tissue. The metabolism and/or clearance of nitroxide from the organism is not related to the redox activity of the tissues and physiological fluids and should be negligible during short-term scanning.

The hydrophilic nitroxides are characterized by a long lifetime in the circulation and a very slow penetration or no penetration into the cells. In contrast, the hydrophobic (and amphiphilic) nitroxides are characterized by a short lifetime in the circulation and an easy penetration into the EES and cells. Therefore, only the hydrophobic cell-penetrating nitroxides are appropriate molecular sensors for MRI/EPR imaging of tissue redox activity, especially *in vivo*.

This study aims to clarify the difference between tissue redox activities in different stages of cancer development *in vivo*. For this purpose, we used two cancer models (neuroblastoma- and glioma-bearing mice), blood-brain barrier (BBB)-penetrating and cell-penetrating nitroxide derivatives, and nitroxide-enhanced MRI and EPR spectroscopy.

3

Materials and Methods

Chemicals

2,2,6,6-Tetramethylpiperidine 1-oxyl (TEMPO)-labeled nitrosourea (SLENU) was synthesized according to Gadjeva et al. (38). SLENU is a spin-labeled analog of the conventional anticancer drug 1-(2-chloroethyl)-3-cyclohexyl-1-nitrosourea (CCNU; Lomustine). 4-Hydroxy-2,2,6,6-tetramethylpiperidine 1-oxyl (TEMPOL) was purchased from Sigma-Aldrich (cat. No. 176141).

Cancer models and experimental design

All experiments were conducted in accordance with the guidelines of the Physiological Society of Japan and were approved by the Animal Care and Use Committee of the National Institute of Radiological Sciences, Chiba, Japan.

The mice (nude *Balb/c*; male) were separated into the following groups: healthy mice (controls) and cancer-bearing mice with brain neuroblastoma or glioma. In all groups, the mice were of identical age, nearly identical weight (23 ± 3 g), and maintained under identical conditions.

Two cancer models were developed using *Neuro2a* (neuroblastoma) or *U87* (glioma) cells. Cancer cells (0.5×10^5 cells in 10 μL) were grafted in one hemisphere of the brain. Anatomically visualized brain neuroblastoma or glioma developed within approximately 9 or approximately 20 days after inoculation, respectively.

The mice were subjected to MRI measurements on the 3rd and 9th day after the inoculation of *Neuro2a* cells or on the 7th and 20th day after inoculation of *U87* cells, when the cancer was in the early and intermediate/terminal stage of its development, respectively.

In preliminary experiments, we investigated the effect of "sham tumor inoculation" (using 10 μL of phosphate-buffered saline (PBS)) on the dynamics of the nitroxide-enhanced MRI signal. Because there was no difference between inoculated and noninoculated hemispheres, or between untreated healthy mice and mice with "sham tumor inoculation," we used untreated healthy mice as controls in this study.

In vivo MRI measurements

MRI measurements were performed on a 7.0 Tesla horizontal magnet (Kobelco and Jastec, Japan) interfaced to a Bruker Avance console (Bruker BioSpin, Germany) and controlled with the ParaVision 4.0.1 program (Bruker BioSpin, Germany).

The mice were anesthetized by isoflurane (1.2%) and placed in a head or body holder (RAPID Biomedical, Germany). A respiration sensor (SA Instruments, Inc., NY, USA) was placed on the back of the mice. A temperature probe (FOT-M and FTI-10, FISO Technologies Inc., Germany) was used to monitor the rectal temperature. The tail vein was cannulated using a polyethylene tube (PE-10, Becton-Dickinson, NJ, USA) for the drug injection. The mouse was placed in the ^{1}H- volume radio-frequency (RF) resonator (Bruker BioSpin) with surface RF receiver (RAPID Biomedical, Germany), which was prewarmed using a body temperature controller (RAPID Biomedical). The resonator units, including the mouse, were placed in the magnet bore. The body temperature was maintained at $37\pm1°C$ during the MRI measurements.

Five control images of the mouse brain or body were taken before injection with the following parameters: T_1-weighted incoherent gradient-echo sequence (fast low-angle shot; FLASH), repetition time = 75 ms; echo time = 3.5 ms; flip angle = 45 degrees; field of view = 3.2 x 3.2 cm; number of averages = 4; scan time = 19.6 seconds; matrix = 64 x 64; slice thickness = 1.0 mm; and number of slices = 4. A solution of nitroxide derivative [SLENU,

4

dissolved in DMSO; or TEMPOL, dissolved in 10 mM PBS, pH 7.4, and reduced by ascorbate, 1:1, mol:mol; 100 mM stock solutions] was injected via the tail vein (100 μL per 25 g mouse; 0.4 μmol/g b.w.) 1 min 40 sec after beginning the scan. T_1-weighted images were acquired continuously within approximately 14 min, using the parameters described above. Mice injected with DMSO served as negative controls. DMSO did not act as a radical scavenger under the experimental conditions described above. TEMPOL, dissolved in DMSO, produced an identical nitroxide-enhanced MRI signal (as intensity and profile) in anesthetized mice as TEMPOL dissolved in PBS. The final dose of each nitroxide was lower than the LD_{50} value calculated for i.v. administration in wild-type mice (38).

The MRI data were analyzed using *ImageJ* software (National Institutes of Health, MD, USA). The averaged value of the first five control sequences (recorded before injection) was calculated, and each sequence of the kinetic measurement was normalized to this averaged value by division using an identical algorithm to that presented by Zhelev et al. (39).

In vitro EPR measurements

The mice were euthanized, and the brain, lung and liver were isolated. The tissues were homogenized in a 4-fold volume of PBS. Protein concentration was measured using the Bradford method, and each homogenate was diluted to 10 mg protein/mL. Noncontrast-enhancing reduced TEMPOL (dissolved in 10 mM PBS, pH 7.4, and reduced by ascorbate; 1:1, mol:mol) was added to the tissue homogenate (final concentration of TEMPOL: 10 mM). The sample (100 μL) was placed into a glass capillary, and X-band EPR spectra were recorded on an X-band EPR instrument (Bruker) with a TE-mode cavity. The measurements were performed under the following conditions: microwave frequency = 9.4 GHz; magnetic field strength = 336 mT; microwave power = 2.0 mW; field modulation frequency = 100 kHz; field modulation amplitude = 0.063 mT; time constant = 0.01 sec; sweep width = 10 mT; and scan time (sweep time) = 1 min (39). The EPR spectra were recorded before and after the addition of reduced TEMPOL. The data were normalized to 1 mg protein/mL.

In vitro total antioxidant capacity assay

The total antioxidant capacity in isolated tissue homogenates was analyzed using the OxiSelect^{TM} Total Antioxidant Capacity Assay Kit (Cell Biolabs, Inc.), according to the manufacturer's instructions. The samples were analyzed photometrically at 490 nm using the microplate reader "Tecan Infinite F200 PRO" (Tecan Austria GmbH).

Analysis of plasma MMP2 and MMP9 levels

The plasma samples were obtained from healthy and neuroblastoma-bearing mice. Enzyme-linked immunosorbent assay (ELISA) was used to determine plasma total MMP2 and total MMP9 levels, according to the manufacturer's instructions. The MMP2 ELISA kit (Human/Mouse/Rat MMP2 [total], Quantikine; R&D Systems Inc., USA) detects pro-, active, and tissue inhibitor of metalloproteinase (TIMP)-complexed MMP2. The MMP9 ELISA kit (Mouse MMP9 [total], Quantikine; R&D Systems Inc.) detects pro-, active, and TIMP-complexed MMP9.

Statistical analysis

The data were statistically analyzed by ANOVA using Student's *t*-test.

Results

Early stage of brain neuroblastoma

Figure 2 shows typical images of the extracted nitroxide-enhanced MRI signal (normalized to the baseline) in healthy (A) and neuroblastoma-bearing mice in the early stage of cancer (3

5

days after inoculation of cancer cells into the brain) (B). In this stage, the tumor cannot be detected anatomically even with high resolution MRI [Spin-Echo (SE) sequence]. The images from both experimental groups were similar. The averaged kinetic curves, however, demonstrated that there was a significant difference in the duration and half-life ($\tau_{1/2}$) of the nitroxide-enhanced MRI signal between control and neuroblastoma-bearing mice (Figure 2C, D).

Two ROIs were selected: (i) the brain area (ROI1) and (ii) the surrounding (nonbrain) area (ROI2) (Figure 2A-a). In both ROIs, the signal increased after the injection of nitroxide followed by a rapid or slower decrease to the baseline. The enhancement of the MRI signal in the beginning is due to the presence of nitroxide in the blood and its penetration and accumulation in the subsequent tissue, whereas the decrease is due to its reduction to noncontrast hydroxylamine, which occurs predominantly in cells.

In the brain area (ROI1) of healthy mice, the half-life of the nitroxide-enhanced MRI signal ($\tau_{1/2}$) was approximately 80 sec and the duration of the signal was ~5 min 40 sec, and these values can be considered a reference for the tissue redox activity of the normal brain (Figure 2C, gray curve). The profile of the histograms indicates a high reducing activity of normal brain tissue for the nitroxide radical. In ROI1 of neuroblastoma-bearing mice, $\tau_{1/2}$ was approximately 56 sec and the duration of the signal was ~3 min, which is significantly shorter than that of control mice (p<0.05) (Figure 2C, red curve). This result indicates that the reducing capacity of the brain tissue in the early stage of brain neuroblastoma was higher than that of the control brain.

In the surrounding (nonbrain) tissues (ROI2), the opposite tendency was observed (Figure 2D). In healthy mice, the half-life of the MRI signal was significantly shorter than that in the neuroblastoma-bearing mice: approximately 82 sec versus approximately 140 sec, respectively (p<0.01). The duration of the signal in neuroblastoma-bearing mice was over 14 min versus 5 min 40 sec min in healthy mice. This result indicates that the reducing activity of nonbrain tissues in the early stage of neuroblastoma is lower than that in the control group. In neuroblastoma-bearing mice, the MRI signal did not reach the baseline within 14 min of continuous scanning (Figure 2D, blue curve), which indicates that the oxidation of nitroxide dominates over reduction.

Terminal stage of brain neuroblastoma
In the terminal stage of brain neuroblastoma (9 days after inoculation), the kinetics of the nitroxide-enhanced MRI signal in the brain and nonbrain tissues were completely different from the reference profiles, recorded for the control group, and from the profiles of the early neuroblastoma group (Figure 3B,C). Three ROIs were selected: (i) the cancerous hemisphere (ROI1); (ii) the noncancerous hemisphere (ROI2); and (iii) the surrounding (nonbrain) area (ROI3) (Figure 3A-a). The cancer was visualized anatomically by MRI.

In ROI1 and ROI2, the signal increased after injection and reached a plateau without a decrease within 14 min ($\tau_{1/2}$ >14 min; p<0.001 vs. control). In ROI3, the signal increased after injection than decreased slowly without reaching the baseline within 14 min ($\tau_{1/2}$ ~14 min; p<0.001 vs. control). The histograms indicate a high oxidative activity of the cancerous and noncancerous tissues of neuroblastoma-bearing mice for the nitroxide. In all ROIs of neuroblastoma-bearing mice, the duration of the signal was over 14 min versus 5 min 40 sec in controls.

The kinetics of the MRI signal demonstrated identical profiles in both hemispheres of the neuroblastoma-bearing brain (Figure 3B); however, the signal intensity was significantly higher in the cancerous area than in the noncancerous hemisphere (Figures 3A, 2B).

6

Early stage of brain glioma

Figure 4A shows a typical image of brain glioma in the early stage of development (9 days after the inoculation of cancer cells into the brain). The tumor is very small but can be visualized anatomically using high-resolution MRI (SE sequence). Two ROIs were selected: (i) the brain area (ROI1) and (ii) the surrounding (nonbrain) area (ROI2) (Figure 4A).

In ROI1 of glioma-bearing mice, the half-life of the MRI signal decay was significantly shorter than that in control mice (~63 sec versus 80 sec, respectively; p<0.05); the duration of the signal was ~3 min versus ~5 min 30 sec in controls (Figure 4B, red curve). This result indicates that the reducing activity of the brain tissue in the early stage of brain glioma is higher than that of the control brain.

In the surrounding tissues (ROI2), an opposite tendency was observed (Figure 4C). In healthy mice, the half-life of the MRI signal was significantly shorter than that in the glioma-bearing mice: approximately 82 sec versus approximately 180 sec, respectively (p<0.01). The duration of the signal in glioma-bearing mice was over 14 min versus ~5 min 40 sec in control mice. This result indicates that the reducing activity of nonbrain tissues in the early stage of brain glioma is lower than that in the control group. In glioma-bearing mice, the MRI signal did not reach the baseline within 14 min of continuous scanning (Figure 4C, blue curve), which indicates that the oxidation of nitroxide dominates over reduction.

Terminal stage of brain glioma

In the terminal stage of brain glioma (20 days after inoculation), the kinetics of the nitroxide-enhanced MRI signal in the brain and nonbrain tissues were completely different from the reference profiles that were recorded for the control group (Figures 5B, 4C). Three ROIs were selected: (i) the cancerous hemisphere (ROI1); (ii) the noncancerous hemisphere (ROI2); and (iii) the surrounding (nonbrain) area (ROI3) (Figure 5A-a). The cancer was visualized anatomically by MRI.

In ROI2, the signal increased after injection and reached a plateau without a decrease within 14 min ($\tau_{1/2}$ >14 min; p<0.001 vs. control). In ROI1 and ROI3, the signal increased after injection then decreased slowly without reaching the baseline within 14 min (in ROI3: $\tau_{1/2}$ ~440 sec; p<0.001 vs. control; in ROI2: $\tau_{1/2}$ ~330 sec; p<0.001 vs. control). The histograms indicate a high oxidative activity of the cancerous and noncancerous tissues of glioma-bearing mice for the nitroxide.

The kinetics of the MRI signal demonstrated identical profiles in both hemispheres of the glioma-bearing brain. However, the signal intensity was significantly higher in the cancerous area than in the noncancerous hemisphere (Figure 5A-b).

Tissue oxidizing capacity *in vivo* and *in vitro*

To verify the data from the nitroxide-enhanced MRI *in vivo*, we utilized a second experimental strategy that employed an oxidized form of nitroxide (Figures 2-5). Nitroxide (TEMPOL) was reduced until there was a complete loss of the MRI and EPR contrast. The reduced noncontrast-enhancing form was injected in anesthetized mice (healthy and cancer-bearing), and the dynamics of the nitroxide-enhanced MRI signal were detected under identical conditions, as in Figures 2 and 3.

The data in Figure 6A indicate that the nitroxide-enhanced MRI signal appeared and increased within 14 min of continuous scanning only in the brain of neuroblastoma-bearing mice in the terminal stage of cancer (red and yellow curves). The signal intensity was higher in the cancerous hemisphere than in the noncancerous hemisphere. In the controls and early stage neuroblastoma, the nitroxide-enhanced MRI signal was not detected (violet and gray curves). The kinetic measurements obtained with injection of oxidized TEMPOL are shown

7

for comparison in Figure 6B. The dynamics were characterized by an initial peak as a result of the accumulation of nitroxide in the brain. For healthy mice or mice with early neuroblastoma, the signal decreased rapidly to the baseline. For mice with terminal neuroblastoma, the signal remained high in both hemispheres.

The results suggest that the noncontrast reduced nitroxide was converted to its contrast-enhancing oxidized form only by the tissues of the neuroblastoma-bearing mice in the terminal stage of cancer. This experimental design proves that these tissues are characterized by high oxidative activity, which is not typical for tissues of healthy mice or neuroblastoma-bearing mice in the early stage of cancer.

Similar data were obtained *in vitro* using tissue specimens (brain, liver and lung) and EPR spectroscopy (Figure 6C). The tissues were isolated from healthy or neuroblastoma-bearing mice in the early or terminal stage of cancer. A reduced noncontrast nitroxide was added to each sample, and the appearance of the EPR spectra was detected after 10 min of incubation at room temperature. The appearance of EPR spectra is a result of the conversion of the nitroxide probe from the reduced to the oxidized (radical) form and is indicative of high oxidative activity of the respective tissue. The EPR triplet appeared in all tissues of neuroblastoma-bearing mice in the terminal stage of cancer and in the liver of neuroblastoma-bearing mice in the early stage of cancer. This result indicates that all of these tissues are characterized by high oxidative activity for the nitroxide probe. The cancerous hemisphere was characterized by the highest tissue oxidative capacity.

Total antioxidant capacity of brain tissue and plasma levels of matrix metalloproteinases
To investigate the potential molecular mechanism(s) of redox imbalance in cancer-bearing mice, we analyzed two biochemical parameters: (i) the total antioxidant capacity (TAC) of brain tissue and (ii) the plasma levels of the matrix metalloproteinases (MMPs) MMP2 and MMP9.

It was established that the total antioxidant capacity of brain tissue slightly increased (~20%) in the early stage of cancer, whereas in the terminal stage, it markedly decreased (~40%) in comparison with the control (Figure 7A). The plasma total MMP2 and MMP9 levels were significantly higher in neuroblastoma-bearing mice in the terminal stage of cancer than those in healthy mice (Figure 7B). The plasma MMP9, but not MMP2, level also increased in neuroblastoma-bearing mice in the early stage of cancer.

Discussion

The data demonstrate two important trends in carcinogenesis: (i) the tissues of cancer-bearing mammals (cancerous and noncancerous, including areas distant from the primary tumor locus) are characterized by high oxidative activity, whereas the tissues of a healthy organism are characterized by high reducing activity for the nitroxide; and (ii) the tissue redox balance is very sensitive to the progression of cancer: in the early stage, reduction dominates over oxidation, whereas in the terminal stage, oxidation dominates over reduction. Our additional experiments on colon cancer-grafted mice treated with camptothecin within 3 weeks demonstrated a suppression of tumor growth and significant normalization of tissue reducing potential compared with the placebo group (data to be published elsewhere).

Similar results have reported by Matsumoto et al. and Hyodo et al. (22, 23). The authors have investigated the dynamics of the nitroxide-enhanced MRI signal in cancer-bearing mice injected with TEMPOL (partially water soluble, BBB-penetrating, and cell-penetrating), carbamoyl-PROXYL (water soluble, partially BBB-penetrating, and partially cell-penetrating) or carboxy-PROXYL (water soluble, BBB nonpenetrating, and cell

8

nonpenetrating). The tumor was grafted in the right hind paw of C3H mice, and the left hind paw was used for comparison. The authors found that the intensity of the nitroxide-enhanced MRI/EPR signal in the noncancerous hind paw was significantly smaller than that in the cancer-bearing hind paw (22), which is similar to our observations (Figure 3A). The authors do not provide data about the MRI/EPR signal decay in healthy mice. They have calculated that the rate of the MRI signal decay of TEMPOL and carbamoyl-PROXYL in cancerous tissue is more rapid than in noncancerous tissue of cancer-bearing mice. However, the ROI covers the central portion of the tumor (tumor core) (22). It is very difficult for water-soluble and even partially hydrophobic substances to penetrate the tumor core, especially within a short time (within 15-20 min) and without a specific transport mechanism. In our studies, we observed a significant difference in the intensity and duration of the nitroxide-enhanced MRI signal between the tumor core and periphery in the terminal stage of cancer (data are not shown). In the tumor core, the signal enhancement was usually negligible even after the injection of cell-penetrating nitroxide (e.g., TEMPOL or SLENU). It is unclear whether the absence of a signal was a result of the rapid reduction of nitroxide or an inability to penetrate the tumor core. In this study, our ROI covers the entire cancer area, which minimizes the effect of different penetration and distribution of nitroxide in different parts of tumor (Figure 2-5).

Most likely, for water-soluble nitroxides (such as carbamoyl-PROXYL and carboxy-PROXYL), the tumor is visualized predominantly on the basis of angiogenesis and the prolonged circulation of nitroxides in the bloodstream and/or prolonged retention in the EES of cancerous tissue. In this case, the MRI signal decay should be a result of nitroxide reduction in the bloodstream and/or EES and clearance from the organism through the kidneys. The same authors have shown that nitroxide-enhanced MRI signal appears first in kidney and after that in cancer area after injection of carboxy-PROXYL (23). Our previous report indicates that the penetration of nitroxide in cells and tissues is obligatory for MR imaging of the cancer based on the tissue redox activity (20).

Even when the BBB is disrupted (as in brain cancer), the water-soluble nitroxides are accumulated and retained in the EES instead of penetrating the cells. This is a major contrast mechanism for the visualization of tumors using water-soluble Gd contrast agents.

In our study, we used SLENU, which is a strongly hydrophobic drug [octanol/PBS partition coefficient (Log $P_{Oct/PBS}$) was 1.000 versus 0.575 for TEMPOL, -0.158 for carbamoyl-PROXY, and -2.000 for carboxy-PROXYL]. Nitrosoureas are well-known DNA annealing agents, penetrating plasma and even nuclear membranes (35, 40). Thus, the dynamics of the nitroxide-enhanced MRI signal using SLENU (Figures 2-5) could be attributed to its penetration into the cells and subsequent intracellular reduction/oxidation.

Recently, Davis et al. have reported that the dynamic of nitroxide-enhanced MRI is very heterogeneous in different tissues of the same cancer-bearing organism (24). We also established that the intensity, half-life and duration of nitroxide-enhancement were different in brain tissue, tissues around the brain, and muscle tissue of the hind paw (Figures 3-5) (21, 39). Moreover, different cancerous tissues (e.g., glioma and neuroblastoma) showed heterogeneous dynamic of nitroxide-enhanced MRI (Figure 3A vs. 5B). Heterogeneity of the signal existed in the same cancerous tissue using different cell-penetrating nitroxide probes: SLENU or TEMPOL (Figures 5, 6). Therefore, the different rates of MRI signal decay could be a result of overlaping of several processes occuring simultaneously in tissues: different penetration rates, different reduction rates, different retention time, and different excretion rates of nitroxide from different tissues.

The different interpretations of the experimental data from the nitroxide-enhanced MRI studies that are published in the literature can be explained by several reasons: (i) the use of nitroxides with different cell-penetrating ability, place of retention, and excretion rate; (ii) the

9

heterogeneity of the signal in different tissues (as a result of their different structure and metabolism); (iii) the heterogeneity of the signal in same tissue for different cell-penetrating nitroxide probes (as a result of their different pharmacokinetics); and (iv) the different analytical approaches (conclusions based on: rate of MRI signal decay; half-life of nitroxide-enhanced MRI signal; and intensity of nitroxide-enhanced MRI signal) (19-24).

Each of the previous interpretations is correct, but none of them takes into account all factors that may affect the intensity and dynamics of nitroxide-enhanced MRI signal in living organism. To assess whether oxidation dominates over reduction in carcinogenesis or vice versa, it is necessary to compare the intensity and dynamics of nitroxide-enhanced MRI signal (rate of decay or half-life) in the same tissue between two animal species – healthy and cancer-bearing. Only in this case, the penetration, retention, and excretion of nitroxide will occur at approximately same speed in the selected ROI, allowing us to ignore the impact of these factors on the dynamics of the signal. Since the cancerous tissue is completely different (structurally and metabolically) from noncancerous, presumably, the most indicative parameter for its redox activity is the duration of nitroxide-enhanced MRI signal. The presence of long-lived signal in the cancerous tissue, while in healthy tissues it is on baseline (Figure 8), is an indicator for the presence of nitroxide in oxidized form, respectively, for the higher tissue oxidative activity in cancer. The results with reduced TEMPOL support this assumption (Figure 6). In the case of reduced TEMPOL, the nitroxide-enhanced MRI signal can appear only if noncontrast hydroxylamine is oxidized to contrast-enhancing nitroxide radical. The data showed that nitroxide-enhancement appeared only in neuroblastoma-bearing brain in terminal stage, but not in healthy brain or neuroblastoma-bearing brain in early stage of cancer.

Our study also demonstrates that the tissue redox balance is very sensitive to the progression of cancer and can be used as a diagnostic marker of carcinogenesis. In the early stage of cancer, the target tissue is characterized by a high reducing activity, whereas it is characterized by a high oxidative activity in the terminal stage. Carcinogenesis correlates with the redox potential of nontarget surrounding tissues and tissues distant from the tumor. In both stages of cancer development, the oxidative status of noncancerous tissues increases, and they become susceptible to oxidative stress and damage.

What is the potential molecular mechanism(s) of these observations? Our hypothesis assumes that the inoculation of cancer cells in the brain can be considered an "inflammatory signal" (Figure 9) (41, 42). This inoculation leads to a local migration and an activation of a wide variety of immune cells in the target tissue, especially in the microenvironment of the primary tumor locus. This activation may trigger redox imbalance due to the "oxidative burst" of the immune cells and the production and release of ROS/RNS in the grafted area. In turn, this process will activate the antioxidant defense systems in the "inflamed" area as a compensatory mechanism to prevent oxidative stress in the microenvironment of the primary tumor locus (1, 41, 42). Our study demonstrates that the total antioxidant capacity of the cancer-grafted brain slightly increased in the early stage of cancer development (Figure 7A). Because the experiments were conducted on immunodeficient mice (Balb/c nude), the early phase was comparatively short (within 3-4 or 7-9 days for brain neuroblastoma or glioma, respectively). Shortly after inoculation, cell proliferation accelerated after overcoming the immune response, and the solid tumor grew.

The initial redox imbalance and subsequent signal transduction in the grafted area could be a critical regulator of cancer progression. ROS/RNS, produced by the immune cells in the primary tumor locus, could provoke signal transduction in three targets with equal probability: (i) the grafted cancer cells; (ii) the surrounding normal cells; and (iii) the surrounding extracellular matrix.

10

ROS/RNS have emerged as important mediators of signal transduction that are associated with the activation of the integrin pathway and modulation of integrin function through conformational changes (43). The cross-talk between cancer cells and the extracellular matrix also activates integrin-related signal cascades. The oncogenic miRNAs, secreted by cancer cells into the environment, are considered a primary mediator of this process (44, 45). The activation of integrins is linked to additional ROS/RNS production by NADPH oxidases, lipoxygenases, mitochondria, etc., leading to a vicious cycle (46). As a result, the antioxidant defense system crashes with the progression of cancer and tissue redox balance shifts towards oxidation in the intermediate/terminal phase (Figure 7A).

Integrin signaling also facilitates cell proliferation and migration, which is intimately linked to the degradation of the extracellular matrix, and activated matrix metalloproteinases are a prerequisite for cancer cell invasion (46). We established that the plasma level of MMP9 increases approximately 2 times even in the early stage of cancer development and approximately 3.5 times in the terminal stage (Figure 7B). The plasma level of MMP2 also increases significantly in the terminal stage of cancer.

Cancer cells are adapted to the high levels of ROS/RNS and survive. However, the normal surrounding cells and extracellular matrix are not adapted to the abnormal free radical attack and can undergo irreversible changes. Our study also indicates that an antioxidant deficiency develops in tissues distant from the cancer locus of a cancer-bearing organism in the terminal stage. These normal tissues become highly sensitive to oxidative damage.

The data suggest that the cancerous and noncancerous tissues of a cancer-bearing organism are equally important therapeutic targets. Combining anticancer therapy with the protection of noncancerous tissues against oxidative stress may be essential for the survival and recovery of the organism.

Disclosure of Potential Conflicts of Interest
No potential conflicts of interest are disclosed.

References
1. Trachootham D, Alexandre J, Huang P. Targeting cancer cells by ROS-mediated mechanisms: a radical therapeutic approach? Nat Rev Drug Discovery 2009;8:579-91.
2. Gius D, Spitz DR. Redox signalling in cancer biology. Antioxid Redox Signal 2006;8:1249-52.
3. Diaz B, Courtneidge SA. Redox signalling at invasive microdomains in cancer cells. Free Radic Biol Med 2012;52:247-56.
4. Irwin ME, Rivera-Del Valle N, Chandra J. Redox control of leukemia: from molecular mechanisms to therapeutic opportunities. Antioxid Redox Signal 2012; Sep 28 [Epub ahead of print].
5. Ziech D, Franco R, Pappa A, Panayiotidis MI. Reactive oxygen species (ROS)-induced genetic and epigenetic alterations in human carcinogenesis. Mutat Res 2011;711:167-73.

11

6. Zienolddiny S, Ryberg D, Haugen A. Induction of microsatellite mutations by oxidative agents in human lung cancer cell lines. Carcinogenesis 2000;21:1521-6.

7. Trachootham D, Lu W, Ogasawara MA, Del Valle NR, Huang P. Redox regulation in cell survival. Antioxid Redox Signal 2008;10:1343-74.

8. Kroemer G, Pouyssegur J. Tumour cell metabolism: cancer's Achilles' heel. Cancer Cell 2008;13:472-82.

9. Kagan V, Bakalova R, Karakashev P. Lipid peroxidation in the tumour cells and tissues of tumour-bearing animals. In Vigo-Pelfrey C, editor. Membrane Lipid Oxidation. CRC Press; Volume III, 1992: p. 191-208.

10. Gupta SC, Hevia D, Patchva S, Park B, Koh W, Aggrawal BB. Upsides and downsides of ROS for cancer: The roles of ROS in tumourogenesis, prevention, and therapy. Antioxid Redox Signal 2012;16:1295-1322.

11. Mandal S, Lindgren AG, Srivastava AS, Clark AT, Banerjee U. Mitochondrial function controls proliferation and early differentiation potential of embryonic stem cells. Stem Cells 2011;29:486-95.

12. Fulda S, Galluzzi L, Kroemer G. Targeting mitochondria for cancer therapy. Nat Rev Drug Discov 2010;9:447-64.

13. Kroemer G. Mitochondria in cancer. Oncogene 2006;25:4630-2.

14. Sanchez-Arago M, Formentini L, Cuezva M. Mitochondria-mediated energy adaptation in cancer: The H(+)-ATP synthase-geared switch of metabolism in human tumours. Antioxid Redox Signal 2012; Sep 24 [Epub ahead of print].

15. Chan EC, Jiang F, Peshavariya HM, Dusting GJ. Regulation of cell proliferation by NAHDH oxidase-mediated signalling: Potential role in tissue repair, regenerative medicine and tissue engineering. Pharmacol Ther 2009;122:97-108.

16. Hayes P, Knaus UG. Balancing reactive oxygen species in the epigenome: NADPH oxidases as target and perpetrator. Antioxid Redox Signal 2012; Nov 5 [Epub ahead of print].

17. Chaiswing L, Zhong W, Liang Y, Jones DP, Oberley TD. Regulation of prostate cancer cell invasion my modulating of extra- and intracellular redox balance. Free Radic Biol Med 2012;52:452-461.

18. Hamanaka RB, Chandel BS. Mitochondrial reactive oxygen species regulate hypoxic signalling. Curr Opin Cell Biol 2009;21:894-9.

19. Zhelev Z, Bakalova R, Aoki I, Gadjeva V, Kanno I. Imaging of cancer by redox-mediated mechanism: a radical diagnostic approach. Mol BioSystems 2010;6:2386-8.

20. Zhelev Z, Gadjeva V, Aoki I, Bakalova R, Saga T. Cell-penetrating nitroxides as molecular sensors for imaging of cancer in vivo, based on tissue redox activity. Mol BioSystems 2012;8:2733-40.

21. Zhelev Z, Aoki I, Gadjeva V, Nikolova B, Bakalova R, Saga T. Tissue redox activity as a sensing platform for imaging of cancer based on nitroxide redox cycle. Eur J Cancer 2012 [Epub ahead of print].

22. Matsumoto K, Hyodo F, Matsumoto A, Koretsky AP, Sowers AL, Mitchell JB et al. High-resolution mapping of tumour redox status by MRI using nitroxides as redox-sensitive contrast agents. Clin Cancer Res 2006;12:2355-62.

23. Hyodo F, Matsumoto K, Matsumoto A, Mitchell JB, Krishna MC. Probing the intracellular redox status of tumours with magnetic resonance imaging and redox-sensitive contrast agents. Cancer Res 2006;66:9921-8.

24. Davis RM, Matsumoto S, Brnardo M, Sowers A, Matsumoto K, Krishna MC et al. Magnetic resonance imaging of organic contrast agents in mice: capturing the whole-body redox landscape. Free Rad Biol Med 2011;50:459-68.

25. Fuchs J, Groth N, Herrling T, Zimmer G. Electron paramagnetic resonance studies on nitroxide radical 2,2,5,5-tetramethyl-4-piperidin-1-oxyl (TEMPO) redox reactions in human skin. Free Radic Biol Med 1997;22:967-76.

26. Batinic-Haberle I, Reboucas JS, Spasijevic I. Superoxide dismutase mimetics: chemistry, pharmacology, and therapeutic potential. Antioxid Redox Signal 2010;13:877-918.

27. Mehlhorn RJ. Ascorbate- and dehydroascorbic acid-mediated reduction of free radicals in the human erythrocytes. J Biol Chem 1991;266:2724-31.

12

28. Bobko AA, Kirilyuk IA, Grigor'ev IA, Zweier JL, Khramtsov VV. Reversible reduction of nitroxides to hydroxylamines: the roles for ascorbate and glutathione. Free Radic Biol Med 2007;42:404-12.

29. Matsumoto A, Matsumoto K, Matsumoto S, Hyodo F, Sowers AL, Koscielniak JW et al. Intracellular hypoxia of tumour tissue estimated by noninvasive EPR oximetry technique using paramagnetic probes. Biol Pharm Bull 2011;34:142-5.

30. Ui I, Okajo A, Endo K, Utsumi H, Matsumoto K. Effect of hydrogen peroxide in redox status estimation using nitroxyl spin probe. Free Radic Biol Med 2004;37:2012-7.

31. Soule BP, Hyodo F, Matsumoto K, Simone NL, Cook JA, Krishna MC et al. Therapeutic and clinical applications of nitroxide compounds. Antioxid Redox Signal 2007;9:1731-42.

32. Hyodo F, Soule BP, Matsumoto K, Matsumoto S, Cook JA, Hyodo E et al. Assessment of tissue redox status using metabolic responsive contrast agents and magnetic resonance imaging. J Pharm Pharmacol 2008;60:1049-60.

33. Hyodo F, Murugesan R, Matsumoto K, Hyodo E, Subramanian S, Mitchell JB et al. Monitoring redox-sensitive paramagnetic contrast agent by EPRI, OMRI and MRI. J Magn Reson 2008;190:105-12.

34. Rosen GM, Cohen MC, Britigan BE, Pou S. Application of spin traps to biological systems. Free Radic Res Commun 1990;9:187-95.

35. Zhelev Z, Matsumoto K, Gadjeva V, Bakalova R, Aoki I, Zheleva A et al. EPR signal reduction kinetic of several nitroxyl derivatives in blood in vitro and in vivo. Gen Physiol Biophys 2009;28:356-62.

36. Okajo A, Matsumoto K, Mitchell JB, Krishna MC, Endo K. Competition of nitroxyl contrast agents as an in vivo tissue redox probe: Comparison of pharmacokinetics by the bile flow monitoring (BFM) and blood circulating monitoring (BCM) methods using X-band EPR and simulation of decay profiles. Magn Reson Med 2006;56:422-31.

37. Hyodo F, Chuang KH, Goloshevsky AG, Sulima A, Griffiths GL, Mitchell JB et al. Brain redox imaging using blood-brain barrier-permeable nitroxide MRI contrast agent. J Cereb Blood Flow Metab 2008;28:1165-74.

38. Gadjeva V. Structure-based design of nitrosoureas containing tyrosine derivatives as potential antimelanoma agents. Eur J Med Chem 2002;37:295-7.

39. Zhelev Z, Bakalova R, Aoki I, Matsumoto K, Gadjeva V, Anzai K et al. Nitroxyl radicals for labelling of conventional therapeutics and noninvasive magnetic resonance imaging of their permeability for blood-brain barrier: relationship between structure, blood clearance, and MRI signal dynamic in the brain. Mol Pharm 2009;6:504-12.

40. Lage H, Dietel M. Involvement of the DNA mismatch repair system in antineoplastic drug resistance. J Cancer Res Clin Oncol 1999;125:156-65.

41. Kundu JK, Surh Y-J. Emerging avenues linking inflammation and cancer. Free Radic Biol Med 2012;52:2013-37.

42. Paez D, Labonte MJ, Bohanes P, Zhang W, Benhanim L, Ning Y, et al. Cancer dormancy: A model of early dissemination and late cancer recurrence. Clin Cancer Res 2011;18:645-53.

43. Gregg D, de Carvalho DD, Kavacic H. Integrins and coagulation: a role for ROS/redox signalling? Antioxid Redox Signal 2004;6:757-64.

44. Rutnam ZJ, Wight TN, Yang BB. miRNAs regulate expression and function of extracellular matrix molecules. Matrix Biol 2012; E-pub: Nov 15.

45. Dalmay T, Edwards DR. MicroRNAs and the hallmarks of cancer. Oncogene 2006;25:6170-5.

46. Svineng G, Ravuri C, Rikardsen O, Huseby NE, Winberg JO. The role of reactive oxygen species in integrin and matrix metalloproteinase expression and function. Connect Tissue Res 2008;49:197-202.

Figure Legends

Figure 1. Nitroxide redox cycle as a sensing platform for the imaging of tissue redox activity: principle of the method. In vitro studies demonstrate that the nitroxide radical,

13

which is characterized by MRI/EPR contrast enhancement, can be converted to the noncontrast-enhancing hydroxylamine and/or oxoammonium by different compounds in cells and body fluids (e.g., free ions of transition metals, hydroxyl and hydroperoxyl radicals, ubiquinols, NAD(P)H, ascorbate, glutathione, etc.). The contrast-enhancing radical form can be recovered by interaction of hydroxylamine with the superoxide radical at physiological pH (7.4) or interaction of oxoammonium with the superoxide radical at pH<4.5. Thus, the nitroxide-enhanced MRI/EPR signal follows the reduction/oxidation of the nitroxide derivative and indicates the redox status of tissues and body fluids.

Figure 2. Healthy and neuroblastoma-bearing mice (early stage of cancer development). **(A, B)** Typical MR images of healthy brain (A) and neuroblastoma-bearing brain in the early stage of cancer (B): (a) MR image of mouse brain; (b) extracted nitroxide-enhanced MRI signal obtained before (baseline; b) and after injection of nitroxide (SLENU; c, d, e). **(C, D)** Kinetics of the nitroxide-enhanced MRI signal in the brain (ROI1) (C) and surrounding (nonbrain) tissues (ROI2) (D) obtained before and after injection of SLENU. Control kinetics (gray dotted lines) obtained in healthy mice are given for comparison. The data are the mean ± SD from 10 animals for the control group and 7 animals for the neuroblastoma-bearing group. ROIs are indicated by dotted lines on MR images. SLENU was in the oxidized (radical) form.

Figure 3. Healthy and neuroblastoma-bearing mice (terminal stage of cancer development). **(A)** Typical MR images of neuroblastoma-bearing brain in the terminal stage of cancer: (a) MR image of mouse brain; (b) extracted nitroxide-enhanced MRI signal obtained before (baseline; b) and after injection of nitroxide (SLENU; c, d, e). **(B, C)** Kinetics of the nitroxide-enhanced MRI signal in the brain, cancerous hemisphere (ROI1) and noncancerous hemisphere (ROI2) (B), and surrounding (nonbrain) tissues (ROI3) (C) obtained before and after injection of SLENU. Control kinetics (gray dotted lines) obtained in healthy mice are given for comparison. The data are the mean ± SD from 10 animals for each group. ROI are indicated by dotted lines on MR images. SLENU was in the oxidized (radical) form.

Figure 4. Healthy and glioma-bearing mice (early stage of cancer development). **(A)** Typical MR image of glioma-bearing mouse brain in the early stage of cancer: (a) MR image of mouse brain; (b) extracted nitroxide-enhanced MRI signal obtained 6 min after injection of nitroxide (SLENU). **(B, C)** Kinetics of the nitroxide-enhanced MRI signal in the brain (ROI1) (B) and surrounding (nonbrain) tissues (ROI2) (C) obtained before and after injection of SLENU. Control kinetics (gray dotted lines) obtained in healthy mice are given for comparison. The data are the mean ± SD from 10 animals for the control group and 5 animals for the glioma-bearing group. ROIs are indicated by dotted lines on the MR image. SLENU was in the oxidized (radical) form.

Figure 5. Healthy and glioma-bearing mice (terminal stage of cancer development). **(A)** Typical MR image of glioma-bearing mouse brain in the terminal stage of cancer: (a) MR image of mouse brain; (b) extracted nitroxide-enhanced MRI signal obtained 6 min after injection of nitroxide (SLENU). **(B, C)** Kinetics of the nitroxide-enhanced MRI signal in the brain, cancerous hemisphere (ROI1) and noncancerous hemisphere (ROI2) (B), and surrounding (nonbrain) tissues (ROI3) (C) obtained before and after injection of SLENU. Control kinetics (gray dotted lines) obtained in healthy mice are given for comparison. The data are the mean ± SD from 10 animals for the control group and 7 animals for the glioma-bearing group. ROIs are indicated by dotted lines on the MR image. SLENU was in the oxidized (radical) form.

Figure 6. Analysis of the tissue oxidizing capacity *in vivo* and *in vitro* in healthy and neuroblastoma-bearing mice in the early and terminal stage of cancer. (A) Kinetics of the nitroxide-enhanced MRI signal in the brain before and after injection of reduced nitroxide

14